Inorganic Chemistry

Article

pubs.acs.org/IC

2H-$CuScO_2$ Prepared by Low-Temperature Hydrothermal Methods and Post-Annealing Effects on Optical and Photoelectrochemical Properties

Thomas I. Draskovic, Mingzhe Yu, and Yiying Wu*

Department of Chemistry & Biochemistry, The Ohio State University, 100 West 18th Avenue, Columbus, Ohio 43210, United States

Supporting Information

ABSTRACT: The delafossite structured $CuScO_2$ is a p-type, wide band gap oxide that has been shown to support significant oxygen intercalation, leading to darkened color and increased conductivity. Control of this oxidation proves difficult by the conventional high-temperature solid-state syntheses. In addition, a pure hexagonal (2H) or rhombohedral (3R) polytype of $CuScO_2$ requires careful control of synthetic parameters or intentional doping. Lower-temperature hydrothermal syntheses have thus far led to only a mixed 2H/3R product. Herein, control of hydrothermal conditions with the consideration of copper and scandium hydrolysis led to the synthesis of light beige, hierarchically structured particles of 2H-$CuScO_2$. Absorption of the particles in the visible range was found to increase upon annealing of the sample in air, most likely due to the Cu^{II} formation from oxygen interstitials. X-ray photoelectron spectroscopy confirmed purely Cu^{I} in the as-synthesized 2H-$CuScO_2$ and increased Cu^{II} amounts upon annealing. Oxidation of the samples also led to shifts of the Fermi level toward the valence band as observed by increases in the measured flat band potentials versus normal hydrogen electrode, confirming increased hole carrier densities.

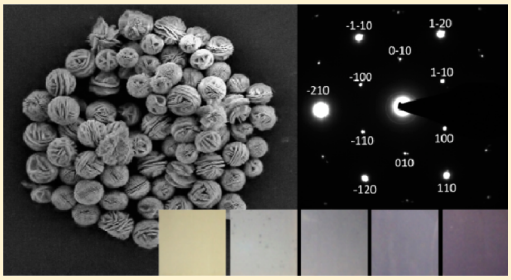

INTRODUCTION

Cuprous delafossite oxides have gained significant attention since the first demonstration of $CuAlO_2$ as a potential p-type transparent conducting oxide.[1] While the conductivities and mobilities can actually be quite limited,[2] the potential applications range from use as thermoelectric materials,[3] electro/photocatalysts,[4−9] transparent p−n junctions,[10−12] and photovoltaic cathodes.[13−22] Their properties stem from a unique structure with alternating layers of linearly coordinated $O-Cu^{I}-O$ and $M^{III}O_6$ edge-shared octahedra. The layers can adopt ABCABC or ABABAB stacking, to give the compounds either a rhombohedra (3R) or hexagonal (2H) symmetry.[23] Concerning the optical properties, Cu^{I} has a closed-shell d^{10} configuration, and contrary to Cu_2O, the two-dimensional Cu−Cu plane weakens or eliminates orbital interactions.[24] Hence, the factors that may reduce the band gap are minimized. When this is combined with an M^{III} species that has a d^0 or d^{10} valence electron configuration (Al, Ga, In, Sc, Y, La), the resulting compound can be transparent in the visible range, with a large optical band gap (>3.2 eV).

$CuScO_2$ has a valence band consisting of mostly Cu^{I} d^{10} orbitals and a conduction band of Sc^{III} d^0 and O p orbitals. The direct-allowed band gap has been determined to be between 3.3−3.7 eV based on calculation and experimental data.[25−28] Like other cuprous delafossite oxides, it exhibits p-type conductivity through a small polaron hopping mechanism localized at the copper site.[29,30] A hole mobility of 2.0×10^{-1} $cm^2\ V^{-1}\ s^{-1}$ and conductivities reaching 30 S cm^{-1} have been reported.[26,27] Relatively high conductivities are able to be achieved through the susceptibility of $CuScO_2$ to both extrinsic acceptor doping and oxygen interstitials.[31] Delafossite oxides with Sc^{III} or B-sites of larger ionic radii are able to support significant oxygen intercalation within the plane of Cu atoms.[26,32−34] For $CuScO_2$, oxygen intercalation has been found to occur more slowly in the 2H polytype, with oxygen being held tighter in the 3R form.[35] Thermogravimetric analysis showed significant mass increases above ∼300 °C, with decomposition to Cu_2O, CuO, and Sc_2O_3 at 600 °C. Rietveld refinement of neutron diffraction data revealed O^{2-} to be in the plane of Cu^{I}. Doping by either an extrinsic acceptor or oxidation darkened $CuScO_2$ samples, with reported colors ranging from white (synthesized in vacuum-sealed tube) to dark blue-gray.[26]

Cuprous delafossites present several synthetic challenges, the most obvious being control of copper's oxidation state. Cu^{I} is unstable at high temperatures until above ∼900 °C, so temperatures greater than ∼900 °C and specific control of heating/cooling rates can be critical in conventional solid-state methods.[36,37] Typical syntheses for $CuScO_2$ include solid-state reaction of the binary components[26,35,38] and metathesis reactions,[35,39,40] with thin films often prepared by various deposition techniques.[25,26,41,42] In each of these methods, high temperatures, controlled atmospheres, and/or vacuum are required to produce light colored, pure 3R or 2H $CuScO_2$ with minimal oxidation. More recent synthetic studies of

Received: March 13, 2015
Published: May 13, 2015

ACS Publications © 2015 American Chemical Society

DOI: 10.1021/acs.inorgchem.5b00575
Inorg. Chem. 2015, 54, 5519−5526

$CuScO_2$ performed by the Poeppelmeier group improved upon earlier hydrothermal syntheses of several delafossites by using a hydrothermal Teflon-pouch method.[43−45] This method allowed for low temperatures (<210 °C), control over hydrolysis of the reactants, and could be applied to many delafossite compounds. The following reaction was attempted at 210 °C for 60 h with 2.5 M NaOH:

$$Cu_2O(s) + 2Sc(OH)_3(s) \rightarrow 2CuScO_2(2H, 3R) + 3H_2O(l)$$

However, consistent with previous solid-state syntheses, pure 2H or 3R phase was difficult to achieve, and only a mixed 2H, 3R sample was obtained. Sample washing with dilute acid was also necessary to remove ScOOH impurities.[43−45]

In this work the hydrothermal synthesis of $CuScO_2$ is revisited using a modified ethylene glycol-assisted hydrothermal synthesis. Through consideration and careful control of the hydrolysis of Cu^I and Sc^{III} species, a pure, single hexagonal polytype $CuScO_2$ was obtained. Large surface area, hierarchical structures were formed, and the as-synthesized beige powder had minimal oxidation of the Cu^I. The optical and photoelectrochemical properties of the pure and oxidized product were investigated.

EXPERIMENTAL METHODS

Materials. Copper(II) nitrate (hemi)pentahydrate (98.0%, Sigma-Aldrich), scandium(III) nitrate hydrate (99.9%, Sigma-Aldrich), potassium hydroxide (90%, Sigma-Aldrich), ethylene glycol (99.0%, Sigma-Aldrich), deionized water (ρ = 18 MΩ·cm, Barnstead E-Pure), aqueous ammonia solution (29.0%, Fisher Scientific), argon (99.998%, Praxair, Inc.), sodium sulfate (99.3%, Fisher Scientific), and sodium hydroxide (98.8%, Fisher Scientific) were used without further purification.

Hydrothermal Synthesis. A modified hydrothermal synthesis was used for $CuScO_2$ based on previous literature.[46] Equimolar amounts of copper and scandium nitrates (5 mmol) were dissolved in deionized water and 3 mL of ethylene glycol. The pH of the solution was adjusted to 3.2 using KOH. The final solution, with a volume of 13.8 mL, was placed in a 23 mL Teflon-lined stainless steel autoclave (Parr Instrument Company). The sealed autoclaves were heated at 210 °C for 60 h. After reaction, the precipitates were collected by centrifugation and washed several times with water. If necessary, dilute ammonium hydroxide was used to remove any copper impurities. The powders were dried overnight at 60 °C in a vacuum oven before characterization.

Film Preparation. Polycrystalline films of $CuScO_2$ were prepared on fluorine-doped tin oxide (FTO) coated glass slides (TEC 7, Hartford Glass Co., Inc.). The slides were first cleaned by sonication in detergent solution (Decon Contrex AP), water, ethanol, and acetone. A final 20 min treatment in an ultraviolet ozone cleaner (Novoscan Technologies, Inc.) was performed. The powders were dispersed in a 1:1 ethanol/water mixture to make a paste, which could then be doctor-bladed on Scotch tape masked FTO slides. After drying at 100 °C, the films were annealed at 500 °C under argon, followed by a final annealing at various temperatures in air to control oxidation of the $CuScO_2$.

Characterization Methods. Products were characterized by powder X-ray diffraction (PXRD) with a Rigaku Corp. Geigerflex using Cu Kα_1 radiation. Lattice parameters were refined using the CELREF software.[47] Scanning electron microscopy (SEM) images were obtained with an FEI/Philips Sirion Field Emission SEM. Transmission electron microscopy (TEM) images and selected-area diffraction patterns were obtained with an FEI/Philips CM-200, while high-resolution TEM (HRTEM) images were obtained with an FEI Titan3. For TEM, the sample powder was dispersed in isopropanol and dropped on a Au grid; small plate fragments from the sample were imaged. Ultraviolet−visible (UV−vis) diffuse reflectance spectra were collected on a PerkinElmer Lambda 950 spectrophotometer with a 60 mm integrating sphere and a Spectralon reflectance standard. X-ray photoelectron spectroscopy (XPS) characterization was performed with a Kratos Axis Ultra XPS spectrometer using monochromatic Al Kα radiation at an operating voltage of 12 kV and a current of 10 mA. The sample powder was pressed onto carbon tape on the sample holder, and an electron flood gun was used to avoid surface-charging problems. Spectra fitting was performed with the CasaXPS software according to previously reported parameters, using combined Gaussian−Lorentzian profiles with a Shirley-type background.[48]

Photoelectrochemical measurements were performed on a Gamry Instruments Reference 600 potentiostat. A 435 W Xe lamp with a water IR-filter (Oriel) was used to illuminate the samples with a chopping frequency of 0.05 Hz and a scan rate of ν = 1 mV/s. An aqueous 0.5 M Na_2SO_4 electrolyte solution was adjusted to the desired pH with NaOH. The reference electrode was a Ag/AgCl (saturated KCl) electrode, and platinum mesh was used as the counter electrode. The working electrode was a $CuScO_2$ film on FTO-coated glass. All solutions were purged with argon for at least 30 min before the experiments. Samples were illuminated from the back side.

RESULTS AND DISCUSSION

Hydrothermal Chemistry and Phase Formation of 2H-$CuScO_2$. Hydrothermal synthesis of complex oxides presents a challenge, in that the hydrolysis and oxidation state of two or more metal species must be controlled. Thus, it is difficult to find a universal set of synthetic conditions that can be applied to oxides even of the same family.[44,45] The Poeppelmeier group's "Teflon pouch method" was successfully applied to many delafossite oxides, but $CuScO_2$ yielded mixed 2H, 3R polytypes.[44,45] A high base concentration was necessary to dissolve any appreciable amount of the $Sc(OH)_3$ reactant, and solubility of Cu^I species suffers under these alkaline conditions. Because of this, the products still contained unreacted ScOOH in addition to the mixed polytype $CuScO_2$. In an effort to produce phase pure $CuScO_2$, ethylene glycol-assisted[44] hydrothermal reactions were modified, considering the hydrolysis of both copper and scandium.

Consideration of Cu^I hydrolysis. The Pourbaix diagram for copper was referenced to approximate stable hydrothermal conditions for Cu^I species.[49] At room temperature, Cu^I is not stable at any pH in aqueous solution, easily disproportionating into Cu^0 and Cu^{II}. Increasing temperature expands a wider stable pH region for Cu^I, and at 200 °C, the dominant species will be Cu^I (aq) when the pH < ~6.8. Above this pH, the stable Cu(OH) (aq) has low solubility (~1×10^{-3} to 1×10^{-4} mM) and easily precipitated as Cu_2O. The presence of soluble alcohols (ethylene glycol, ethanol, isopropanol, etc.), which are capable of acting as reducing agents, also further stabilizes Cu^I.

Consideration of Sc^{III} Hydrolysis. Studies on the aqueous geochemistry of metal species are also valuable resources for approximating their behavior under laboratory hydrothermal reaction conditions.[50] At saturated water vapor pressure and typical hydrothermal reaction temperatures of 200−300 °C, $Sc(OH)_2^+$ (aq) is the dominant species in a very narrow range from pH ≈ 3−3.5, then $Sc(OH)_3^0$ (aq) within the broader range of pH ≈ 3.5−7. Considering stability of Cu^I, a pH range of 3−6 should be appropriate for formation of $CuScO_2$. However, under weak acidic conditions, $Sc(OH)_3^0$ can precipitate as the stable ScOOH: $Sc(OH)_3^0$ (aq) → ScOOH (s) + H_2O (l). Because of the broad solubility minimum of ScOOH, moderate acidic conditions should be suitable for the transport of Sc species and reduce unreacted hydroxide impurities.

DOI: 10.1021/acs.inorgchem.5b00575
Inorg. Chem. 2015, 54, 5519−5526

Hydrothermal Synthetic Conditions. With a better understanding of the hydrothermal chemistry of copper and scandium, synthetic conditions could be established for $CuScO_2$. Numerous reactions were attempted with pH adjusted from 2 to 11. Indeed, it was found that only in a narrow range around pH = 3.2 significant formation of $CuScO_2$ occurred. Above this pH, ScOOH would dominate, and attempts at dissolving the impurity with dilute acid also led to dissolution of the $CuScO_2$. Below this pH, various broad diffraction peaks appeared that could not be matched to any particular copper or scandium compounds but were likely amorphous hydroxides (See Figure S1 in the Supporting Information). Therefore, at pH = 3.2, Cu^I is stable, there is suitable transport of Sc^{III} species, and product dissolution is avoided. The addition of ethylene glycol has also been shown to promote cuprous delafossite phase formation, most likely by acting as a reducing agent and lowering the dielectric constant of the solution.[46] Ethylene glycol (3 mL, 22% v/v) was found to best minimize the amount of unreacted ScOOH. Similar to the Teflon pouch method, a temperature of 210 °C was used to lower dielectric constant of water, and a reaction time of 60 h ensured full reaction of Cu^I with any poorly soluble ScOOH. The proposed reactions are therefore

$$Cu^+(aq) + Sc(OH)_2{}^+(aq) \rightarrow CuScO_2(s) + 2H^+(aq)$$

$$Cu^+(aq) + Sc(OH)_3{}^0(aq) \rightarrow CuScO_2(s) + H_2O(l) + H^+(aq)$$

$CuScO_2$ Phase Characterization. To confirm the phase purity of samples, PXRD was performed. Figure 1 shows the

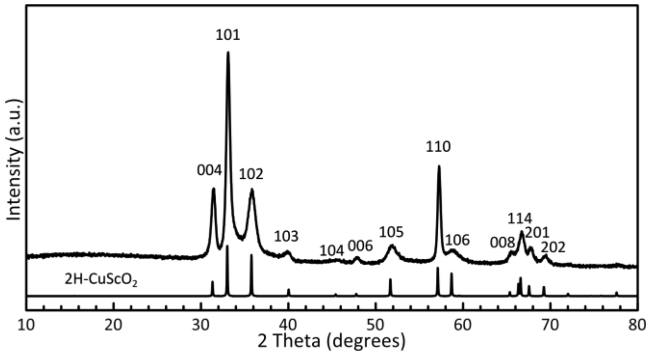

Figure 1. Indexed PXRD pattern of 2H-$CuScO_2$ with calculated $P6_3/mmc$ reference pattern.

diffraction pattern of the $CuScO_2$ obtained from the optimized hydrothermal synthetic conditions. Interestingly, the peaks match well with only with hexagonal $P6_3/mmc$ polytype, with no evidence of the peak broadening that can occur from stacking faults in mixed rhombohedral (3R) and hexagonal (2H) samples.[35] The refined lattice parameters a = 3.218(6) Å and c = 11.384(1) Å also match those previously reported for hexagonal sample prepared by solid-state methods.[26,35,38] The formation of a pure 2H product is significant considering the great difficulty faced in other synthetic methods. Solid-state syntheses have required controlled atmospheres, quenching of the reactions from high temperatures, and/or extrinsic doping to stabilize the 2H polytype; exchange reactions between $LiScO_2$ and CuCl have yielded pure 3R-$CuScO_2$ but require careful handling of CuCl and sealing of evacuated quartz tubes.[26,35,38,40] Aside from controlling the polytype formation, obtaining any delafossite phase by the solid-state methods can prove challenging due to the relative instability of Cu_2O and $M^{III}{}_2O_3$ at lower temperatures, as detailed in a recent study.[37] While careful tuning of pH is required, the reported hydrothermal method can repeatedly produce pure 2H-$CuScO_2$.

XPS was performed on the as-synthesized $CuScO_2$ to verify the chemical states of copper and scandium. Figure 2 provides

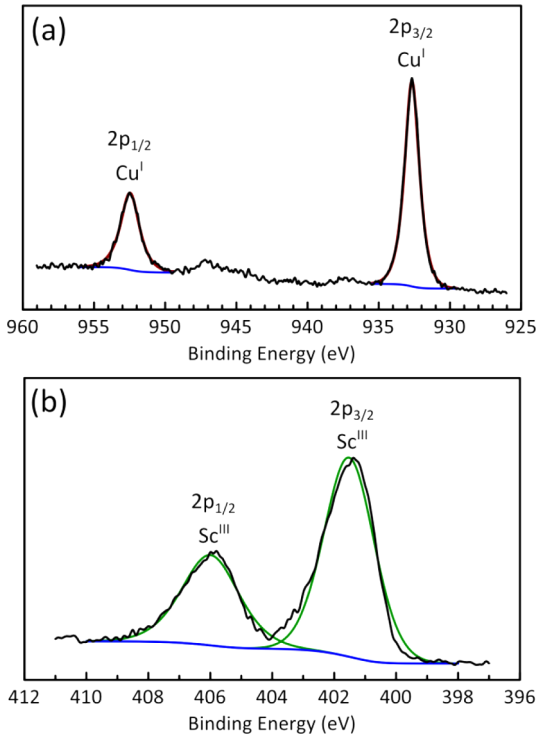

Figure 2. XPS of as-synthesized 2H-$CuScO_2$. (a) Cu 2p. (b) Sc 2p.

the spectra at binding energies corresponding to Cu 2p and Sc 2p. The Cu 2p spectrum indicates a Cu $2p_{3/2}$ peak at 932.7 eV and a Cu $2p_{1/2}$ peak at 952.5 eV. The peak regions were fit well by one component, and the binding energies are consistent with those for Cu^I oxides.[48,51] The Sc 2p spectrum indicates a Sc $2p_{3/2}$ peak at 401.5 eV and a Sc $2p_{1/2}$ peak at 406.0 eV, matching with those previously reported for Sc_2O_3.[48,51] While the peaks could not be fit clearly by single components, attempts to fit with more components did not provide any improvement. Possible explanations for this include a small amount of surface charging or the presence of surface hydroxide groups. Despite this, the Sc 2p spectra were consistent across several samples.

The product morphology was characterized by SEM, as shown in Figure 3. Large hierarchical clusters of plates with diameters from 5 to 10 μm were formed. Similar large clusters, designated as "gypsum flower," were also observed at low pH conditions in the ethylene glycol-assisted synthesis of $CuGaO_2$, but the exact reason for their formation is not well understood.[46] This structure can also explain the slight broadening of X-ray diffraction peaks containing a c-axis component (i.e., (00l) and ($h0l$)), which is likely due to stacking faults at the intersections of these large plates. Closer inspection of the edges of the plates comprising the large clusters shows the attachment of much smaller plates,

DOI: 10.1021/acs.inorgchem.5b00575
Inorg. Chem. 2015, 54, 5519−5526

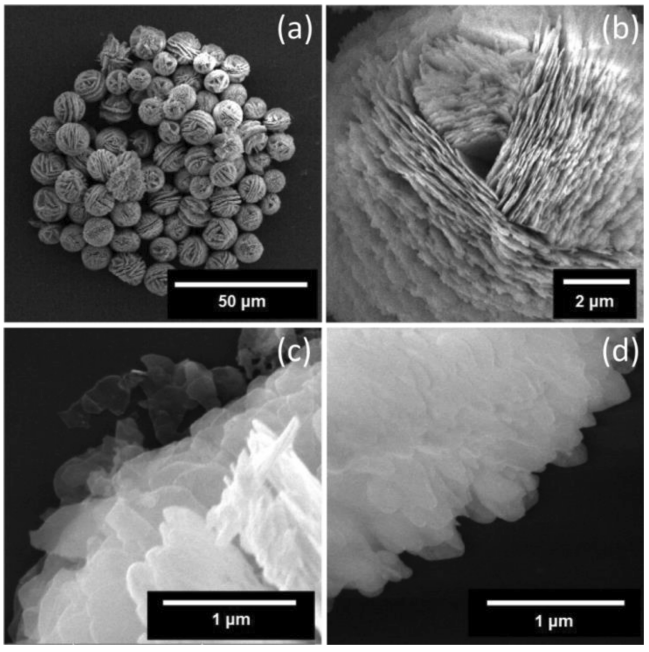

Figure 3. (a, b) SEM images of $CuScO_2$ hierarchical clusters. (c, d) Magnified SEM image of cluster edges, highlighting the attachment of smaller plates.

indicating that the clusters likely grow by the oriented attachment mechanism of the initially formed small plates. This is promising for future attempts as smaller particle synthesis through the control and inhibition of the orientated attachment process.[52]

The smaller plate fragments from the edge of the clusters were isolated for TEM imaging and electron diffraction. Figure 4a,b shows the edge of a clearly hexagonal plate and the indexed selected-area electron diffraction pattern shows the particle's single crystallinity. The HRTEM image of a plate edge

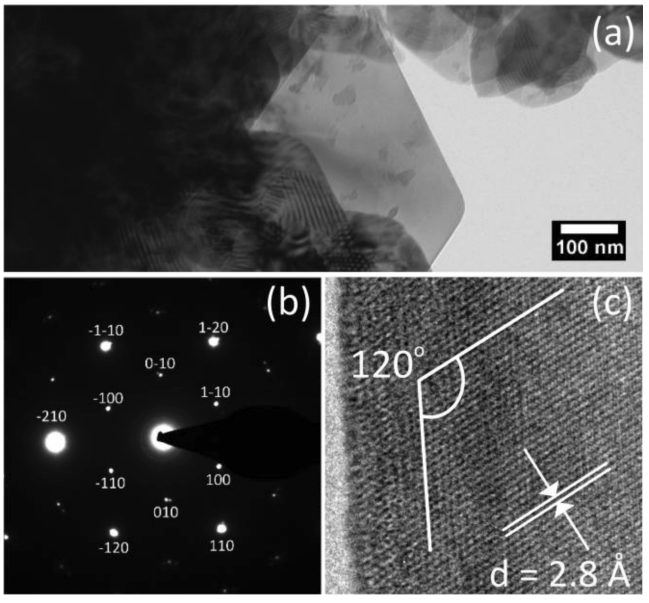

Figure 4. (a) TEM image of $CuScO_2$ plate. (b) Corresponding indexed electron diffraction pattern. (c) HRTEM image of $CuScO_2$ plate edge indicating 120° angle and 2.8 Å lattice spacing viewed along the ⟨001⟩ direction.

shows clear lattice planes with a spacing of ~2.8 Å, closely matching the *d*-spacing between {100} lattice planes. Plates with {001} planes exposed on the top/bottom are consistent with previously reported hydrothermally synthesized 3R-$CuGaO_2$ and $CuCrO_2$ particles.[15,17]

Optical Properties of 2H-$CuScO_2$ Powders. One of the unique properties of $CuScO_2$ is that it is the first in a series of cuprous delafossite oxides susceptible to significant oxygen intercalation without decomposition.[26,34,40,53] The formula of this oxidized compound is typically written as $CuScO_{2+x}$, with x reaching values up to 0.5.[35] Since this oxidation can occur in air at temperatures as low as 250 °C, controlling oxidation during solid-state syntheses has been difficult. Often, a light gray color is obtained, and only in evacuated sealed tubes can nearly colorless samples be obtained.[26,35] The 2H-$CuScO_2$ prepared in this work was a light beige color, and XPS indicated initial low levels of oxidation. If desired, the oxidation can now be controlled through postannealing methods.

UV−vis diffuse reflectance spectroscopy was performed to investigate the optical properties of the freshly prepared $CuScO_2$, as well as postannealed samples. Reflectance data were plotted according to the Kubelka−Munk theory:[54]

$$F(R_\infty) = (1 - R_\infty)^2/2R_\infty$$

where R_∞ is the calibrated sample reflectance. The optical band gaps could further be calculated by considering the energy dependence of the absorption coefficient α near the band gap absorption edge:

$$\alpha h\nu = (h\nu - E_g)^2$$

for a direct-allowed transition, where $\alpha = F(R_\infty)$ assuming the sample scattering coefficient remains constant within the narrow energy range of the absorption.[55] Figure 5 shows the

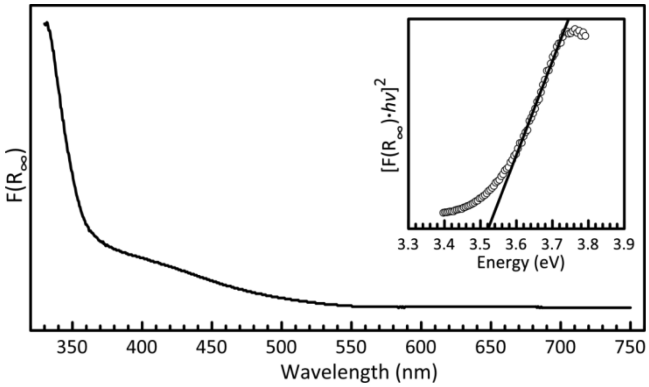

Figure 5. Kubelka−Munk UV−vis diffuse reflectance spectra of as-synthesized 2H-$CuScO_2$. (inset) Absorption edge indicating direct optical band gap of 3.52 eV.

diffuse reflectance Kubelka−Munk absorption and the absorption edge of the as-synthesized $CuScO_2$. The light beige powder had little absorption in the visible range and was calculated to have a direct-allowed band gap of 3.52 eV. While optical properties of bulk powder $CuScO_2$ samples have not been studied, the determined band gap is consistent with previous calculations and experimental data from thin films.[25−28] While there is a clear absorption onset, explanations for the increased absorption around 375−500 nm include the possibility for a broad distribution of surface state energy levels and more simply, the possible reflection of light within the

DOI: 10.1021/acs.inorgchem.5b00575
Inorg. Chem. 2015, 54, 5519−5526

hierarchical clusters resulting in a longer optical path length and greater absorption.

As a wide band gap p-type semiconductor, $CuScO_2$ could have several potential applications in catalysis or photovoltaics. It is likely that in either of these applications an annealing step will be required. For this reason, the influence of annealing under several different conditions on the synthesized $CuScO_2$ absorption and direct band gap was studied. In anticipation of future electrochemical measurements, where good electrical contact between particles is necessary, all samples were annealed at 500 °C under argon atmosphere prior to annealing in air. Figure 6a shows the diffuse reflectance Kubelka–Munk

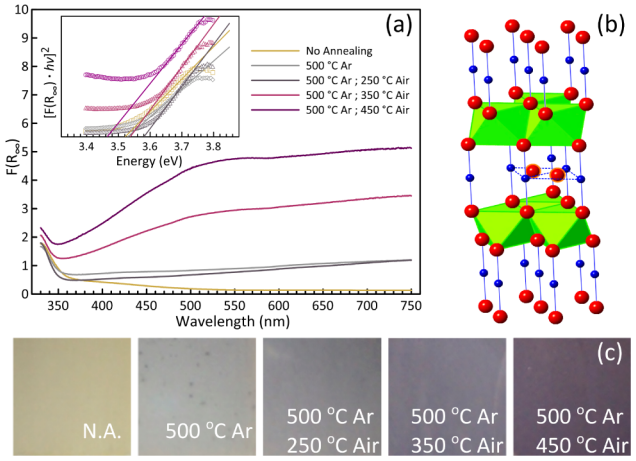

Figure 6. (a) Kubelka–Munk UV–vis diffuse reflectance spectra of annealed 2H-$CuScO_2$ samples. (inset) Corresponding absorption edges. (b) 2H-$CuScO_2$ lattice indicating positions of intercalated oxygen. (c) Digital photographs of annealed samples.

absorption of the as-synthesized $CuScO_2$ and samples annealed at various temperatures. After annealing under argon, the powder turned light gray. Further annealing at 250 °C in air caused a barely detectable change in color. At 350 and 450 °C in air the powders turned dark gray-violet, with a significant increase in absorption around 500 nm. Considering the reported positions of intercalated oxygen into the plane of Cu^I in 2H-$CuScO_2$ (Figure 6b), Cu^I sites are likely oxidized and acquire a nearly square-planar geometry. Recently, calculation of oxygen interstitial formation enthalpies has shown four-coordinate copper sites are stable in the bulk.[56] Thus, this increased absorption can likely be attributed to d–d transitions of Cu^{II}. UV–vis spectroscopy of square-planar Cu^{II} complexes also attribute transitions around 500–550 nm to d–d transitions.[57] The broad increased absorption, particularly extending past 550 nm, could possibly be due to intraband transitions resulting from various oxidized copper or oxygen interstitial states, and again, the reflection of trapped light within the sample resulting in greater absorption. The absorption edges for the direct optical band gaps of the annealed samples are shown in the inset of Figure 6a. At low doping levels (below degeneracy), the optical band gap is expected to remain the same. While the accuracy of fitting the absorption edge can decrease as absorption at energies lower than the band transition increases, the approximated gaps of the annealed samples remain within 0.06 eV of the as-synthesized sample. XRD patterns of the annealed samples indicated no clear changes in peak position or shape (Figure S2 of the Supporting Information). The relative thinness of the plates that formed the hierarchical clusters may help to reduce any strain within the lattice due to intercalated oxygen.

X-ray Photoelectron Spectroscopy of Oxidized 2H-$CuScO_2$. To explicitly show the increased oxidation of Cu^I to Cu^{II} upon annealing, XPS was performed on the various annealed $CuScO_2$ samples. The Cu 2p spectra are shown in Figure 7. With increased annealing temperature, the Cu $2p_{3/2}$

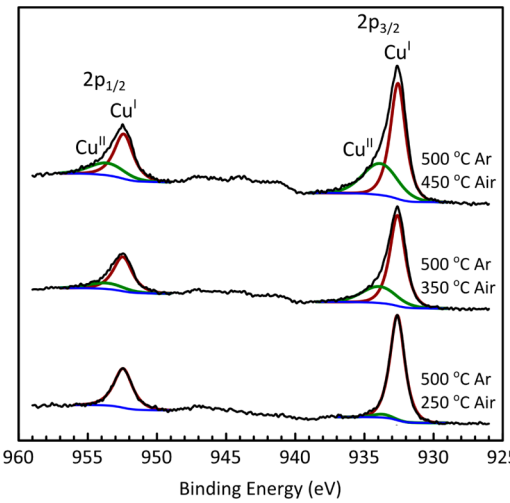

Figure 7. Cu 2p X-ray photoelectron spectra of annealed 2H-$CuScO_2$.

and Cu $2p_{1/2}$ peaks broaden. Two distinct new components were fitted at 933.8 and 953.6 eV for Cu^{II} $2p_{3/2}$ and Cu^{II} $2p_{1/2}$, respectively. In addition, the characteristic Cu^{II} $2p_{3/2}$ satellite peaks from 940–945 eV appeared and increased in intensity.[48,51] Satellite peaks occur when an outgoing core electron excites a valence electron to a higher energy level, reducing the kinetic energy of the core electron. Since these electrons are part of the total Cu 2p emission, the Cu $2p_{3/2}$ peak and corresponding satellite peak areas could be used to estimate the ratio of Cu^I/Cu^{II}.[48] Only the 500 °C Ar, 450 °C annealed $CuScO_2$ had sufficient Cu^{II} satellite peak intensity to allow for appropriate fitting of each component. The fitted Cu $2p_{3/2}$ spectra is shown in Figure S3 of the Supporting Information. Using the combined peak areas, it was estimated that 42.4% of the Cu^I was oxidized to Cu^{II}, corresponding to the formula $CuScO_{2.21}$. This estimation assumes every oxygen interstitial is paired around a copper site, leading to a formal oxidation state of 2+. A distribution of oxidation states is likely, considering the possibility of isolated oxygen interstitials, so the assignment of purely Cu^I and Cu^{II} may lead to an underestimation in the oxygen content. For all samples in this work, the Sc 2p, O 1s, and C 1s spectra remained similar.

***E_{fb}* Measurements of Oxidized 2H-$CuScO_2$ Films.** The increased intercalated oxygen content in $CuScO_2$ by thermal oxidation has been shown to increase conductivity due to increased hole charge carrier density (p):[26,30,27]

$$0.5O_2(g) \leftrightarrow O_i'' + 2h\bullet$$

$$p = 2[O_i'']$$

Increases in hole charge carrier density result in lowering of the Fermi level toward the valence band maximum in a semiconductor. Experimentally, the Fermi level can be estimated by determination of the flat-band potential (E_{fb}) at a semiconductor-electrolyte interface. If a potential bias is

DOI: 10.1021/acs.inorgchem.5b00575
Inorg. Chem. 2015, 54, 5519–5526

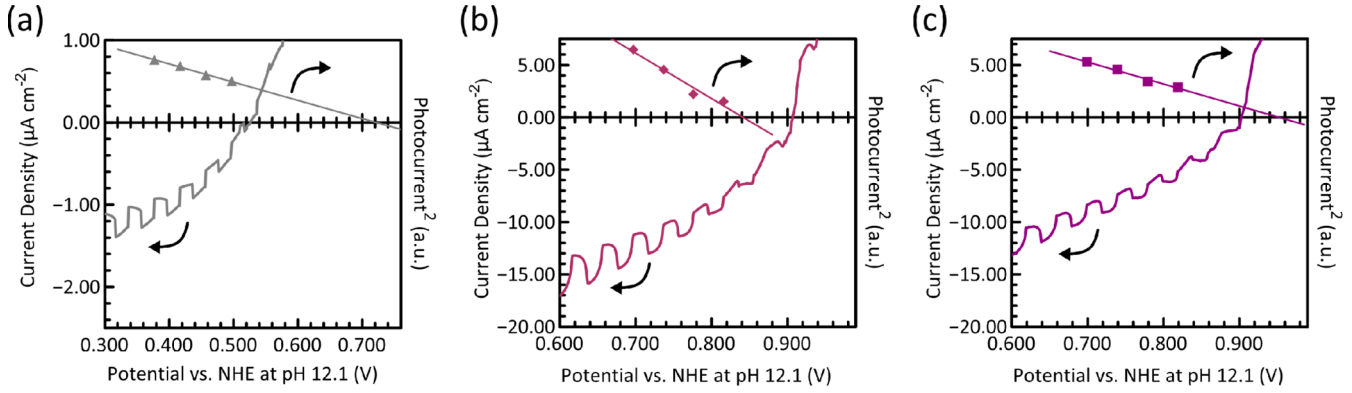

Figure 8. Chopped-light linear sweep voltammograms (left-side axes) and photocurrent onset potentials (right-side axes) of annealed $CuScO_2$ films in aqueous 0.5 M Na_2SO_4 solution (pH = 12.1). 500 °C Ar, 250 °C Air; E_{fb} = 0.721 V (a). 500 °C Ar, 350 °C Air; E_{fb} = 0.845 V (b). 500 °C Ar, 450 °C Air; E_{fb} = 0.938 V (c).

applied to a p-type semiconductor in contact with an electrolyte such that no space charge layer exists in the semiconductor, the conduction and valence bands are flat at the semiconductor-electrolyte interface, and the applied potential is equal to E_{fb}. As more negative bias is applied to the semiconductor electrode, its Fermi level moves toward less negative values of energy (in solid-state vacuum scale), and the bands bend downward. In the dark, this establishes a barrier to charge transfer, and no current flows. Upon illumination with radiation at higher energy than the band gap of the semiconductor, electron−hole pairs are generated, and the electrons in the conduction band travel through the interface toward the electrolyte, generating a cathodic photocurrent. Thus, the onset of photocurrent corresponds to the flat-band potential value.

Figure 8 shows the measurement of E_{fb} in a 0.5 M Na_2SO_4 aqueous solution (pH adjusted to 12.1). The light source was a 435 W Xe lamp, and its output was chopped with a mechanical chopper with a frequency of 50 mHz. As the potential bias to the semiconductor was increased toward more negative values, the current under illumination became more negative (i.e., cathodic). This confirmed $CuScO_2$ to be a p-type semiconductor. The photocurrent onset value was obtained by using the Butler method to calculate E_{fb} according to the following equation:[58]

$$i_{ph}^{\ 2} \propto (E - E_{fb})$$

where i_{ph} is the photocurrent and E is the applied potential bias. According to this equation, the intercept of the linear region of $i_{ph}^{\ 2}$ versus E plot with the x-axis will be E_{fb}, as shown in Figure 7 ($i_{ph}^{\ 2}$ plotted on the right-side axes). Indeed, photocurrent increased, and the E_{fb} was shifted to more positive potentials versus normal hydrogen electrode: 0.721, 0.845, and 0.938 V for the 250, 350, and 450 °C films, respectively. The PEC behavior and photocurrent response of the film without an air annealing was negligible, likely due to the $CuScO_2$ being too insulating (i.e., low charge carrier density due to limited oxygen interstitials). A pH of 12.1 was chosen for the aqueous electrolyte to avoid dissolution of the $CuScO_2$ and for the lack of clear oxidative and reductive peaks in cyclic voltammograms (see Figures S4 and S5 in the Supporting Information).

With the large solubility of oxygen interstitials in $CuScO_2$, increases in carrier density resulting in Fermi level shifts are not surprising. Using the Cu^{II} amount determined from XPS, the hole carrier density was estimated to be ~4.13×10^{21} cm^{-3}. Comparing this density to a reported undoped $CuScO_2$ carrier density (~5×10^{18} cm^{-3}) gave an E_F shift of 172 mV.[30] Considering the limitations in both the XPS determination of the Cu^{II} amount and the photocurrent onset method for flat band determination, a difference between the estimated and measured shifts can be expected. Regardless, the shifts are of the same magnitude.

Unfortunately, the increases in flat-band potential for the $CuScO_2$ films investigated in this work came at the cost of transparency in the visible range, one of the most attractive properties of the delafossite oxides. For transparent conducting oxide applications, future work on controlling particle size and film preparation, as well as a detailed investigation of oxygen intercalation and the nature of defect states in the hydrothermally prepared delafossite particles, will be necessary.

■ CONCLUSION

$CuScO_2$ was synthesized by low-temperature ethylene glycol-assisted hydrothermal techniques. PXRD and electron diffraction confirmed that the $CuScO_2$ was pure hexagonal $P6_3/mmc$. Reported solid-state techniques required precise control of stoichiometry and temperature to obtain pure rhombohedral or hexagonal polytypes, while previous hydrothermal techniques have led to mixtures of the hexagonal and rhombohedral polytypes. The as-synthesized hierarchical clusters were light beige in color with minimal absorption in the visible range, and XPS indicated no oxidation of the copper sites. Oxidation of the 2H-$CuScO_2$ in air at temperatures up to 450 °C gave darkened powders with absorption in the visible range likely due to the increased Cu^{II} content from intercalated oxygen, as shown by XPS. Increasing interstitial oxygen also supported the positive shift seen in the flat band potential as determined by the photocurrent onset of the various oxidized $CuScO_2$ films. The reported hydrothermal synthesis provides future opportunities for extrinsic acceptor doping to increase conductivity and the potential for morphology control. Investigation of these modified syntheses and a more detailed study of the photocathodic stability of the $CuScO_2$ are currently underway.

■ ASSOCIATED CONTENT

Ⓢ Supporting Information

PXRD patterns of the products from varied pH hydrothermal syntheses; PXRD patterns of annealed $CuScO_2$; Cu $2p_{3/2}$ XPS spectrum of the 500 °C Ar, 450 °C annealed 2H-$CuScO_2$; cyclic voltammograms of $CuScO_2$ films in aqueous 0.5 M

DOI: 10.1021/acs.inorgchem.5b00575
Inorg. Chem. 2015, 54, 5519−5526

Na_2SO_4 solution (pH = 12.1); and PXRD patterns of $CuScO_2$ film before and after photoelectrochemical testing. The Supporting Information is available free of charge on the ACS Publications website at DOI: 10.1021/acs.inorgchem.5b00575.

AUTHOR INFORMATION

Corresponding Author

*E-mail: wu@chemistry.ohio-state.edu.

Author Contributions

The manuscript was written through contributions of all authors. All authors have given approval to the final version of the manuscript.

Notes

The authors declare no competing financial interest.

ACKNOWLEDGMENTS

The authors acknowledge the funding support from the U.S. Department of Energy (Award No. DE-FG02-07ER46427). H. Colijn and the Ohio State University Center for Electron Microscopy and Analysis (CEMAS) are acknowledged for assistance in the collection of all transmission electron microscopy images and electron diffraction patterns.

REFERENCES

(1) Kawazoe, H.; Yasukawa, M.; Hyodo, H.; Kurita, M.; Yanagi, H.; Hosono, H. *Nature* **1997**, *389*, 939−942.

(2) Ingram, B. J.; Bertoni, M. I.; Poeppelmeier, K. R.; Mason, T. O. *Thin Solid Films* **2005**, *486*, 86−93.

(3) Okuda, T.; Jufuku, N.; Hidaka, S.; Terada, N. *Phys. Rev. B* **2005**, *72*, 144403.

(4) Monnier, J. R.; Hanrahan, M. J.; Apai, G. *J. Catal.* **1985**, *92*, 119−126.

(5) Christopher, J.; Swamy, C. S. *J. Mater. Sci.* **1992**, *27*, 1353−1356.

(6) Ikeda, S.; Tanaka, A.; Hosono, H.; Kawazoe, H.; Hara, M.; Kondo, J. N.; Domen, K. In *Studies in Surface Science and Catalysis;* Hideshi, H., Kiyoshi, O., Eds.; Science and Technology in Catalysis 1998 Proceedings of the Third Tokyo Conference on Advanced Catalytic Science and Technology; Elsevier: Amsterdam, 1999; Vol. *121*, pp 301−304.

(7) Lekse, J. W.; Underwood, M. K.; Lewis, J. P.; Matranga, C. *J. Phys. Chem. C* **2012**, *116*, 1865−1872.

(8) Gu, J.; Wuttig, A.; Krizan, J. W.; Hu, Y.; Detweiler, Z. M.; Cava, R. J.; Bocarsly, A. B. *J. Phys. Chem. C* **2013**, *117*, 12415−12422.

(9) L. Veselovskyi, V.; V. Ischenko, E.; V. Gayday, S.; Byeda, A.; V. Tkach, V.; V. Lisnyak, V. *Curr. Catal.* **2013**, *2*, 7−12.

(10) Yanagi, H.; Ueda, K.; Ohta, H.; Hirano, M.; Hosono, H. *Solid State Commun.* **2001**, *121*, 15.

(11) Jayaraj, M. K.; Draeseke, A. D.; Tate, J.; Hoffman, R. L.; Wager, J. F. In *Symposium F−Transport and Microstructural Phenomena;* MRS Online Proceedings Library, 2001; Vol. *666*.

(12) Hoffman, R. L.; Wager, J. F.; Jayaraj, M. K.; Tate, J. *J. Appl. Phys.* **2001**, *90*, 5763−5767.

(13) Bandara, J.; Yasomanee, J. P. *Semicond. Sci. Technol.* **2007**, *22*, 20.

(14) Nattestad, A.; Zhang, X.; Bach, U.; Cheng, Y.-B. *J. Photonics Energy* **2011**, *1*, 011103−011103 − 9.

(15) Yu, M.; Natu, G.; Ji, Z.; Wu, Y. *J. Phys. Chem. Lett.* **2012**, *3*, 1074−1078.

(16) Renaud, A.; Chavillon, B.; Le Pleux, L.; Pellegrin, Y.; Blart, E.; Boujtita, M.; Pauporté, T.; Cario, L.; Jobic, S.; Odobel, F. *J. Mater. Chem.* **2012**, *22*, 14353.

(17) Xiong, D.; Xu, Z.; Zeng, X.; Zhang, W.; Chen, W.; Xu, X.; Wang, M.; Cheng, Y.-B. *J. Mater. Chem.* **2012**, *22*, 24760.

(18) Xiong, D.; Zhang, W.; Zeng, X.; Xu, Z.; Chen, W.; Cui, J.; Wang, M.; Sun, L.; Cheng, Y.-B. *ChemSusChem* **2013**, *6*, 1432−1437.

(19) Xu, X.; Zhang, B.; Cui, J.; Xiong, D.; Shen, Y.; Chen, W.; Sun, L.; Cheng, Y.; Wang, M. *Nanoscale* **2013**, *5*, 7963−7969.

(20) Xu, Z.; Xiong, D.; Wang, H.; Zhang, W.; Zeng, X.; Ming, L.; Chen, W.; Xu, X.; Cui, J.; Wang, M.; Powar, S.; Bach, U.; Cheng, Y.-B. *J. Mater. Chem. A* **2014**, *2*, 2968−2976.

(21) Yu, M.; Draskovic, T. I.; Wu, Y. *Phys. Chem. Chem. Phys.* **2014**, *16*, 5026.

(22) Ahmed, J.; Blakely, C. K.; Prakash, J.; Bruno, S. R.; Yu, M.; Wu, Y.; Poltavets, V. V. *J. Alloys Compd.* **2014**, *591*, 275−279.

(23) Marquardt, M. A.; Ashmore, N. A.; Cann, D. P. *Thin Solid Films* **2006**, *496*, 146−156.

(24) Buljan, A.; Llunell, M.; Ruiz, E.; Alemany, P. *Chem. Mater.* **2001**, *13*, 338−344.

(25) Duan, N.; Sleight, A. W.; Jayaraj, M. K.; Tate, J. *Appl. Phys. Lett.* **2000**, *77*, 1325.

(26) Nagarajan, R.; Duan, N.; Jayaraj, M. K.; Li, J.; Vanaja, K. A.; Yokochi, A.; Draeseke, A.; Tate, J.; Sleight, A. W. *Int. J. Inorg. Mater.* **2001**, *3*, 265−270.

(27) Kakehi, Y.; Satoh, K.; Yotsuya, T.; Masuko, K.; Ashida, A. *Jpn. J. Appl. Phys.* **2007**, *46*, 4228−4232.

(28) Hiraga, H.; Makino, T.; Fukumura, T.; Weng, H.; Kawasaki, M. *Phys. Rev. B* **2011**, *84*.

(29) Ingram, B. J.; Mason, T. O.; Asahi, R.; Park, K. T.; Freeman, A. J. *Phys. Rev. B* **2001**, *64*, 155114.

(30) Ingram, B. J.; Harder, B. J.; Hrabe, N. W.; Mason, T. O.; Poeppelmeier, K. R. *Chem. Mater.* **2004**, *16*, 5623−5629.

(31) Ingram, B. J.; González, G. B.; Mason, T. O.; Shahriari, D. Y.; Barnabè, A.; Ko, D.; Poeppelmeier, K. R. *Chem. Mater.* **2004**, *16*, 5616−5622.

(32) Cava, R. J.; Zandbergen, H. W.; Ramirez, A. P.; Takagi, H.; Chen, C. T.; Krajewski, J. J.; Peck, W. F., Jr.; Waszczak, J. V.; Meigs, G.; Roth, R. S.; Schneemeyer, L. F. *J. Solid State Chem.* **1993**, *104*, 437−452.

(33) Trari, M.; Töpfer, J.; Doumerc, J. P.; Pouchard, M.; Ammar, A.; Hagenmuller, P. *J. Solid State Chem.* **1994**, *111*, 104−110.

(34) Elazhari, M.; Ammar, A.; Elaatmani, M.; Trari, M.; Doumerc, J. P. *Eur. J. Solid State Inorg. Chem.* **1997**, *34*, 503−509.

(35) Li, J.; Yokochi, A. F. .; Sleight, A. W. *Solid State Sci.* **2004**, *6*, 831−839.

(36) Kumekawa, Y.; Hirai, M.; Kobayashi, Y.; Endoh, S.; Oikawa, E.; Hashimoto, T. *J. Therm. Anal. Calorim.* **2010**, *99*, 57−63.

(37) Amrute, A. P.; Łodziana, Z.; Mondelli, C.; Krumeich, F.; Pérez-Ramírez, J. *Chem. Mater.* **2013**, *25*, 4423−4435.

(38) Köhler, B. U.; Jansen, M. *Z. Anorg. Allg. Chem.* **1986**, *543*, 73−80.

(39) Doumerc, J.-P.; Ammar, A.; Wichainchai, A.; Pouchard, M.; Hagenmuller, P. *J. Phys. Chem. Solids* **1987**, *48*, 37−43.

(40) Park, S.; Keszler, D. A. *J. Solid State Chem.* **2003**, *173*, 355−358.

(41) Kakehi, Y.; Nakao, S.; Satoh, K.; Yotsuya, T. *Thin Solid Films* **2003**, *445*, 294−298.

(42) Zhao, Q.; Zhao, X.; Sleight, A. W.; Li, J. In *International Symposium on Photonic Glass;* International Society for Optics and Photonics: Bellingham, WA, 2003; pp 248−253.

(43) Shannon, R. D.; Rogers, D. B.; Prewitt, C. T. *Inorg. Chem.* **1971**, *10*, 713−718.

(44) Sheets, W. C.; Mugnier, E.; Barnabé, A.; Marks, T. J.; Poeppelmeier, K. R. *Chem. Mater.* **2006**, *18*, 7−20.

(45) Sheets, W. C.; Stampler, E. S.; Bertoni, M. I.; Sasaki, M.; Marks, T. J.; Mason, T. O.; Poeppelmeier, K. R. *Inorg. Chem.* **2008**, *47*, 2696−2705.

(46) Srinivasan, R.; Chavillon, B.; Doussier-Brochard, C.; Cario, L.; Paris, M.; Gautron, E.; Deniard, P.; Odobel, F.; Jobic, S. *J. Mater. Chem.* **2008**, *18*, 5647.

(47) Laugier, J.; Bochu, B. *CELREF (Version 3);* Grenoble INP: Grenoble, France, 2015.

(48) Biesinger, M. C.; Lau, L. W. M.; Gerson, A. R.; Smart, R. S. C. *Appl. Surf. Sci.* **2010**, *257*, 887−898.

(49) Beverskog, B. *J. Electrochem. Soc.* **1997**, *144*, 3476.

(50) Wood, S. A.; Samson, I. M. *Ore Geol. Rev.* **2006**, *28*, 57−102.

DOI: 10.1021/acs.inorgchem.5b00575
Inorg. Chem. 2015, 54, 5519−5526

(51) *NIST X-ray Photoelectron Spectroscopy Database*, Version 4.1; National Institute of Standards and Technology: Gaithersburg, MD, 2012. http://srdata.nist.gov/xps/.
(52) Yu, M.; Draskovic, T. I.; Wu, Y. *Inorg. Chem.* **2014**, *52*, 5845−5851.
(53) Li, J.; Yokochi, A.; Amos, T. G.; Sleight, A. W. *Chem. Mater.* **2002**, *14*, 2602−2606.
(54) Kubelka, P. *J. Opt. Soc. Am.* **1948**, *38*, 448.
(55) Barton, D. G.; Shtein, M.; Wilson, R. D.; Soled, S. L.; Iglesia, E. *J. Phys. Chem. B* **1999**, *103*, 630−640.
(56) Amrute, A. P.; Łodziana, Z.; Mondelli, C.; Krumeich, F.; Pérez-Ramírez, J. *Chem. Mater.* **2013**, *25*, 4423−4435.
(57) Amundsen, A. R.; Whelan, J.; Bosnich, B. *J. Am. Chem. Soc.* **1977**, *99*, 6730−6739.
(58) Butler, M. A. *J. Appl. Phys.* **1977**, *48*, 1914−1920.

DOI: 10.1021/acs.inorgchem.5b00575
Inorg. Chem. 2015, 54, 5519−5526